Received 18 November 2023, accepted 29 November 2023, date of publication 7 December 2023, date of current version 13 December 2023.

Digital Object Identifier 10.1109/ACCESS.2023.3340420

RESEARCH ARTICLE

Cooperative HARQ-Aided Multiple UAVs in Optical Aerospace Backhaul Networks

KHANH D. DANG[1], (Student Member, IEEE), HOANG D. LE[2], (Member, IEEE), CHUYEN T. NGUYEN[1], AND ANH T. PHAM[2], (Senior Member, IEEE)

[1]School of Electrical and Electronic Engineering, Hanoi University of Science and Technology, Hanoi 100000, Vietnam

[2]School of Computer Science and Engineering, The University of Aizu, Aizuwakamatsu 965-8580, Japan

Corresponding author: Chuyen T. Nguyen (chuyen.nguyenthanh@hust.edu.vn)

The work of Hoang D. Le was supported in part by the Japan Society for the Promotion of Science (JSPS) KAKENHI under Grant 23K19124. The work of Anh T. Pham was supported in part by JSPS KAKENHI Grant 21K11870.

ABSTRACT With the growing demand for high-speed connectivity and global coverage in future 6G networks, free-space optics (FSO)-based aerospace integrated networks, incorporating low Earth orbit (LEO) satellites, high-altitude platforms (HAP), and unmanned aerial vehicles (UAV), have recently attracted research efforts worldwide. Nevertheless, critical challenges on FSO links include weather conditions, atmospheric turbulence, and pointing misalignment. This paper addresses the design of error-control protocols for reliable FSO-based aerospace backhaul networks, when multiple UAVs are deployed as flying base stations (BSs). Specifically, we introduce a design proposal of a cooperative hybrid automatic repeat request (C-HARQ)-based frame allocation mechanism (FAM)/rate adaptation. The design proposal guarantees the latency fairness constraints among multiple UAVs experiencing varying turbulence channel conditions. An analytical channel model for HAP-aided relaying LEO satellite to the emerging UAV-mounted BS FSO links is provided. Moreover, we develop a comprehensive analytical framework taking into account the imperfect channel state information (CSI) to assess system performance metrics, including throughput, average frame delay, and energy efficiency. Numerical results confirm the effectiveness of our design proposal by comparing it with the conventional approach without FAM for various turbulence channel conditions and quality of service (QoS) requirements. Additionally, we offer a design guideline for the proper selection of parameters that can be helpful for the practical design of reliable FSO-based aerospace backhaul networks. Finally, the theoretical results are verified by Monte-Carlo simulations, along with some in-depth discussions.

INDEX TERMS Aerospace backhaul networks, free-space optics (FSO), UAV-mounted BS, cooperative HARQ, frame allocation mechanism, rate adaptation, imperfect CSI.

I. INTRODUCTION

Recently, extensive research efforts have been dedicated to the development of sixth-generation (6G) wireless networks, with the involvement of both academia and industry [1]. Aerospace integrated network, incorporating satellites, high-altitude platforms (HAP), and unmanned aerial vehicles (UAV), is the key architecture for 6G networks [2]. This architecture guarantees seamless and ubiquitous access services, especially in remote, hotspot, or emergency areas, which are uncovered or less covered by the ground base stations (BSs). With the increasing popularity of low Earth orbit (LEO) satellite projects such as SpaceX's Starlink, OneWeb, Telesat, and Iridium, the incorporation of HAPs as relay stations augments the scalability of satellite systems [3]. On the other hand, UAVs offer significant advantages, e.g., cost-effectiveness, rapid deployment, low latency, and robust line-of-sight connections, making them potential aerial

The associate editor coordinating the review of this manuscript and approving it for publication was Halil Ersin Soken.

access points for ground users [4]. As a result, the aerospace integrated network jointly comprised of the UAV access and LEO satellite/HAP backhaul is a promising framework for future 6G networks.

To fulfill the ever-increasing demand for data rates in next-generation cellular wireless networks, high-frequency bands, including sub-THz (0.1 THz - 1 THz) and free-space optical (FSO) technology, are promising candidates for satellite/HAP backhaul networks [16]. Compared with traditional radio frequency (RF) systems, sub-THz offers several advantages, such as higher bandwidth capacity, increased data rates, and reduced energy consumption. Sub-THz communications nevertheless encounter critical challenges that require extensive effort to render them viable for long-distance connectivity, e.g., in satellite systems. First, the transmissions at sub-THz bands face substantial channel loss (i.e., 1 to tens of dB/km), while the output power level of sub-THz devices is currently restricted to around 1 Watt [17]. Secondly, it is still a significant challenge in fabricating broadband-spectrum, energy-efficient electronic devices operating at sub-THz bands [18]. Restricted electron mobility and considerable signal loss in the doped substrates contribute to the limitation in bandwidth and high noise figures in electronic devices operating at such high frequencies.

On the other hand, FSO communication has gained a reputation for its ability to provide high-speed data services over long distances [19]. Compared to sub-THz links, leveraging the low-loss transmission windows of atmospheric channels (below 0.2 dB/km at specific carrier frequencies) becomes feasible, especially considering that the output power of commercially available semiconductor lasers has already surpassed a few Watts. In addition, FSO can offer massive bandwidth, extremely high data rates, low power consumption, and immunity to electromagnetic interference [20]. The implementation of the FSO backhaul connectivity of LEO satellite-HAP-UAV links is not without challenges. Primary concerns of the FSO-based LEO satellite-to-HAP link are the pointing misalignment and the Doppler effect. It is also challenging for the FSO connection on the second hop between HAP and UAV-mounted BS due to the severe impact of cloud coverage, atmospheric turbulence, and UAV hovering-induced misalignment [21]. These critical issues pose various challenges to the design of FSO-based aerospace backhaul networks, which require much research effort on error-control solutions.

A. RELATED WORK AND MOTIVATION

1) RELATED WORKS

Early framework for FSO-based aerospace integrated backhaul wireless networks was introduced by Alzenad et al. [22]. This study indicated the potential as well as the key challenging issues, i.e., weather and atmospheric turbulence conditions, of FSO vertical backhaul networks. Following this promising proposal, substantial efforts have been devoted to such networks' design and performance evaluation, e.g., [5], [6], [7], [8], [9], [10], [11], [12], [13], [14], and [15]. These studies mainly addressed the issues of (i) network topology formation [5], [6], [7], [8] and (ii) error-control design from both physical-layer [9], [10], [11], [12], [13] and link-layer [14], [15] approaches. As for the error-control design, the existing works have primarily focused on physical-layer solutions, such as hybrid FSO/RF scheme [9], rate adaptation transmission [10], intelligent reflecting surface (IRS)-aided relays [11], [12], and trajectory optimized solution [13]. To further improve the reliability and efficiency of the FSO-based aerospace backhaul networks, recent studies have been dedicated to addressing the design of link-layer retransmission protocols [14], [15]. These studies highlighted the outperformance of cooperative hybrid automatic repeat requests (C-HARQ) compared to other link-layer solutions in FSO-based aerospace-integrated networks. Moreover, the effectiveness of the incremental redundancy (IR) HARQ-based sliding window mechanism was also confirmed in terms of system throughput, latency, and energy efficiency performance.

2) MOTIVATIONS

It is worth noting that the available link-layer error-control solutions for FSO-based aerospace-integrated networks primarily focused on a single user. In practice, deploying multiple optical beams at HAP allows such networks to effectively support multiple UAV-mounted BSs. This, in turn, necessitates the design of novel link-layer error-control solutions. It is because applying the available solutions in [14] and [15] for the context of multiple UAVs is not straightforward and poses critical challenges for two remarkable reasons. Firstly, one of the primary concerns for the link-layer design supporting multiple UAVs is to effectively address the resource allocation issue. This involves taking into account different turbulence channel conditions with varying Quality of Service (QoS) requirements. Secondly, another critical concern of the protocol design is to ensure fairness among different UAVs. This should be carefully addressed to promote equitable resource allocation and enhance user satisfaction. For the aforementioned reasons, it is necessary and essential to develop a novel link-layer error-control design for FSO-based aerospace backhaul networks supporting multiple UAVs. To our best knowledge, such designs are not available in the literature, which motivates us to focus on this study.

B. MAJOR CONTRIBUTIONS AND ORGANIZATION

The primary objective of this paper is to provide *a novel design of a link-layer error-control solution* and *a comprehensive analytical framework* for FSO-based aerospace backhaul networks supporting multiple UAV-mounted BSs. Here, we also boldly and explicitly compare our study with the existing literature in Table 1. In a nutshell, the major contributions of this paper are summarized as follows.

TABLE 1. Related works on FSO-based aerospace integrated backhaul networks.

Works	Network Topology Formation	Error Control Design			
		Physical-layer	*Link-layer*	*Multiple Users*	*Outdated CSI*
[5]–[8]	✓	×			
[9]–[13]	×	✓	×	×	×
[14], [15]	×	×	✓	×	×
Our Study	×	×	✓	✓	✓

TABLE 2. List of main notations.

Parameters	Description
N	Total number of UAVs
$i \in \{1, 2, \cdots, N\}$	Subscript to indicate the i-th UAV
K_i	Total number of modes on $\mathcal{R}$-$\mathcal{D}_i$ link
$k_i \in \{1, 2, \cdots, K_i\}$	Transmission mode k_i for the i-th UAV
$\rho_{\mathrm{CSI},i}$	Correlation Coefficient
$\bar{\tau}_{\mathrm{c}}$	Average cycle duration
C-HARQ with Frame Allocation	
λ_{i,k_i}	Number of frames allocated to the i-th UAV
N_{t}	C-HARQ's persistent level
n_f	Burst size
ψ	Number of frame groups in a burst
δ_{i,k_i}	Number of frames per group
Transceivers and FSO Channels	
$\mathcal{X}$,$\mathcal{Y}$	Denote $\mathcal{S}$, $\mathcal{R}$, and $\mathcal{D}_i$ nodes
$\gamma_{k_i}^{\mathcal{R},\mathcal{D}i}$	SNR thresholds on $\mathcal{R}$-$\mathcal{D}_i$ link
$\theta_{\mathrm{d}}^{\mathcal{X}}$	Divergence angle of the $\mathcal{X}$ node's beam
$P_{\mathcal{X}}$	Transmitted Power of the node $\mathcal{X}$
$H_{\mathcal{X}}$	Altitude of the node $\mathcal{X}$
$\sigma_n^{\mathcal{X},\mathcal{Y}}$	Receiver noise standard deviation
$\xi^{\mathcal{X},\mathcal{Y}}$	Zenith angle between $\mathcal{X}$ and $\mathcal{Y}$
$L^{\mathcal{X},\mathcal{Y}}$	Link distance between $\mathcal{X}$ and $\mathcal{Y}$
$L_{\mathrm{c},i}$	Cloud liquid water content
$M_{\mathrm{c},i}$	Cloud droplet number concentration
$C_n^2(0)$	Ground-level turbulence

TABLE 3. Table of abbreviations.

Abbreviation	Description
6G	Sixth-Generation
ARQ	Automatic Repeat Request
BER	Bit Error Rate
BS	Base Station
C-HARQ	Cooperative Hybrid ARQ
CLWC	Cloud Liquid Water Content
CRC	Cyclic Redundancy Check
CSI	Channel State Information
FAM	Frame Allocation Mechanism
FER	Frame Error Rate
HAP	High-altitude Platform
HARQ	Hybrid Automatic Repeat Request
FSO	Free-Space Optics
IR	Incremental Redundancy
LEO	Low Earth Orbit
QAM	Quadrature Amplitude Modulation
QoS	Quality of Service
RF	Radio Frequency
RS	Reed Solomon
RTD	Round Trip Delay
SAT	Satellite
SNR	Signal-to-Noise Ratio
SR	Selective Repeat
UAV	Unmanned Aerial Vehicle
VLEO	Very Low Earth Orbit

C_1: *It is a proposal to design a novel link-layer retransmission protocol-aided multiple UAV-mounted BSs in FSO-based backhaul networks. Specifically, we introduce the design of a C-HARQ-based frame allocation mechanism (FAM)/rate adaptation. FAM aims to effectively allocate the data frames while ensuring latency fairness constraints among multiple UAVs experiencing varying turbulence channel conditions. To facilitate the C-HARQ-based FAM operation, the rate adaptation scheme is employed to maximize the data rate while satisfying a predefined QoS, e.g., targeted bit error rate (BER).*

From the proposed design, we develop an analytical framework that allows obtaining the system performance metrics, including throughput, average delay, and energy efficiency, in case of imperfect channel state information (CSI).

C_2: *We provide insightful numerical results into the detailed impacts of weather conditions, dynamic FSO channels, and imperfect CSI on the performance of aerospace backhaul networks employing C-HARQ-based FAM/rate adaption. Moreover, we offer a design guideline for the proper parameter selection, which can be helpful for the practical system design.*

The results highlight the effectiveness of the proposed design by comparing it with the conventional approach without FAM. Also, we conduct the simulations to verify the correctness of the model and analysis.

The remainder of this paper is organized as follows. In Section II, we describe the network scenario and the proposal for C-HARQ-based FAM/rate adaptation. The FSO channels of LEO satellite-to-HAP and HAP-to-UAV are characterized in Section III. Section IV focuses on the system performance analysis, including throughput, delay, and energy efficiency. The simulation results are given in Section V. Finally, we conclude the paper in Section VI. For the sake of explicit clarity, the list of main notations used in the analysis and the table of abbreviations are provided in Tables 2 and 3, respectively.

II. SYSTEM DESCRIPTIONS

A. SYSTEM MODEL

The FSO-based vertical backhaul network with multiple UAV-mounted BSs is illustrated in Fig. 1. Particularly, a remote area is connected to the core network via the LEO satellite constellation (e.g., SpaceX's Starlink). Then, the HAP serves as a relay station between the LEO

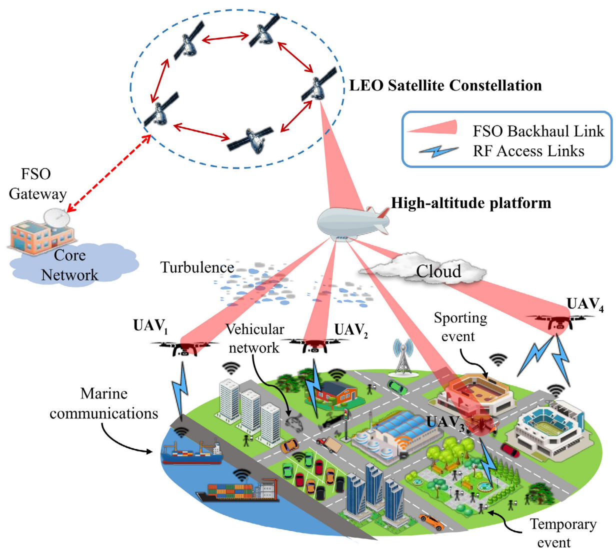

FIGURE 1. Optical aerospace backhaul network with multiple UAV-mounted BSs.

satellite and N UAV-mounted BSs, which provides the RF access links, e.g., for sporting events, vehicular networks, marine communications, and temporary events. In this paper, we focus on the reliability of FSO backhaul links for HAP-aided relaying the LEO satellite to N UAVs For the sake of brevity, we denote the LEO satellite as the $\mathcal{S}$ node, the relay HAP as the $\mathcal{R}$ node, and the UAV as the $\mathcal{D}_i$ node with $i \in \{1, 2, \cdots, N\}$. The decode-and-forward scheme is employed at the $\mathcal{R}$ node, which decodes the data received from the $\mathcal{S}$ before their retransmission to the $\mathcal{D}_i$ node. Also, the $\mathcal{R}$ node is equipped with multiple FSO beams to support multiple $\mathcal{D}$ nodes.

To maintain reliable FSO backhaul links, we employ the C-HARQ-based FAM/rate adaptation. Notably, the objective of C-HARQ protocols is to guarantee the system's reliability by retransmitting redundancies and combining them to correct corrupted data frames. To support multiple UAVs, FAM aims to efficiently allocate data frames while ensuring latency fairness among $\mathcal{D}$ nodes. The frame allocation is determined based on the channel conditions, e.g., clouds and atmospheric turbulence, for which the rate adaptation scheme is used to facilitate the FAM. The purpose of the rate adaptation scheme is to maximize the data rate while satisfying a predefined QoS requirement for the targeted BER. We adopt the subcarrier M-QAM scheme with a fixed symbol rate of R_s for $\mathcal{R}$-$\mathcal{D}_i$ links [23]. For the sake of simplicity, we assume that the feedback channel carrying ACK/NAK signals for C-HARQ-based FAM operation is reliable.

B. FSO CHANNEL MODELS

We now review the FSO channel models for each transmission hop, including LEO satellite-to-HAP and HAP-to-UAV links.

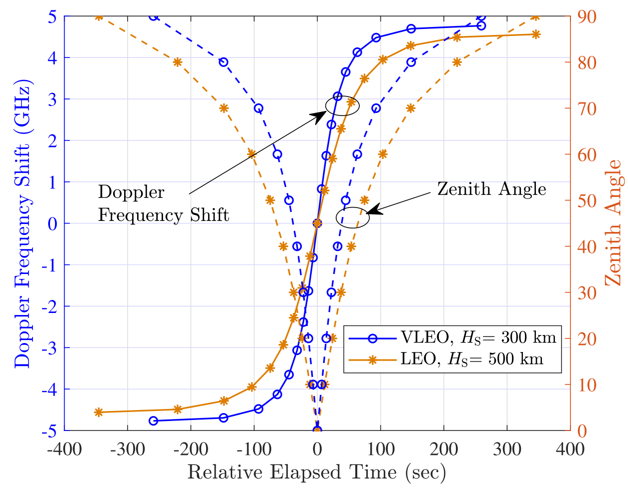

FIGURE 2. Doppler frequency shift and zenith angle versus relative elapsed time.

1) LEO SATELLITE-TO-HAP LINK

As the effect of atmospheric turbulence is negligible above 20 km from the sea level, we investigate (i) *the Doppler effect* and (ii) *the pointing error* for the $\mathcal{S}$-$\mathcal{R}$ link.

As for the Doppler effect, the fast motion of the satellite during the pass produces a Doppler frequency shift at a stable HAP, which is approximated as [24, (1)]

$$f_D \approx f_{opt}\left(\frac{\sqrt{1-\frac{v_S^2}{c^2}}}{1-\frac{v_S}{c}\left(\frac{r_E}{r_E+(H_S-H_R)}\sin\left(\xi^{\mathcal{S},\mathcal{R}}\right)\right)}-1\right), \quad (1)$$

where f_{opt} is the optical carrier frequency, c is the light velocity, and $\xi^{\mathcal{S},\mathcal{R}}$ is the zenith angle. Additionally, v_S is the satellite's velocity determined as $v_S = \sqrt{\frac{\mu_G}{r_E+(H_S-H_R)}}$, where μ_G and r_E are found in [24, Table I], while H_S and H_R are the altitudes of $\mathcal{S}$ and $\mathcal{R}$ nodes, respectively. Given $\beta_S = \arccos\left(\frac{r_E}{r_E+(H_S-H_R)}\sin\left(\xi^{\mathcal{S},\mathcal{R}}\right)\right) - 90^\circ + \xi^{\mathcal{S},\mathcal{R}}$, the relative elapsed time is given as [24, (5)] $\tau_S = (r_E + (H_S - H_R))\frac{\beta_S}{v}$.

Remark 1: Figure 2 depicts the Doppler frequency shift versus the relative elapsed time for different satellite orbits, i.e., LEO and VLEO. As seen, the LEO satellites offer longer communication duration and a less severe impact of Doppler shift compared to VLEO ones. Furthermore, the maximum Doppler frequency shift, approximately ±4.5 GHz, falls within the capability range of the current receiver design for FSO systems, which can effectively handle Doppler shifts up to ±15 GHz as reported in [25]. Therefore, we ignore this effect in our performance analysis.

Regarding the pointing error, the generalized misalignment model between the LEO satellite and the hovering UAV is well described in [15, Section III-A.2]. Given $h_p^{\mathcal{S},\mathcal{R}}$ derived by [15, (8)], the PDF of received signal-to-noise ratio (SNR) at $\mathcal{R}$, denoted as $\gamma^{\mathcal{S},\mathcal{R}}$, is given as [15, (10)]

$$f_{\gamma}^{\mathcal{S},\mathcal{R}}(\gamma^{\mathcal{S},\mathcal{R}}) = \frac{\varphi_{\mathrm{R}}^2}{2\gamma^{\mathcal{S},\mathcal{R}}(A_{\mathrm{R}})^{\varphi_{\mathrm{R}}^2}}\left(\frac{\gamma^{\mathcal{S},\mathcal{R}}}{\Psi^{\mathcal{S},\mathcal{R}}}\right)^{\varphi_{\mathrm{R}}^2/2}, \quad (2)$$

where $\Psi^{S,R} = \frac{\Re_{\mathrm{R}}^2 P_{\mathrm{S}}^2}{(\sigma_n^{S,R})^2}$. Here, $\Re_{\mathrm{R}}$ is the HAP's detector responsivity, P_{S} is the satellite's transmitted power, and $\sigma_n^{\mathcal{S},\mathcal{R}}$ is the receiver noise variance. Additionally, A_{R} and φ_{R}^2 are given in [15, Section III-A.2].

2) HAP-TO-UAV LINK

For the FSO link between HAP and i-th UAV, we consider major impairments, i.e., cloud attenuation $h_{\mathrm{c}}^{\mathcal{R},\mathcal{D}_i}$, atmospheric turbulence $h_{\mathrm{a}}^{\mathcal{R},\mathcal{D}_i}$, and pointing misalignment $h_{\mathrm{p}}^{\mathcal{R},\mathcal{D}_i}$.

As for the cloud attenuation, as reported in [15, Section III-B.1], the power attenuation is given as [15, (11)]

$$h_{\mathrm{c}}^{\mathcal{R},\mathcal{D}_i} = \exp\left(-\zeta_i H_{\mathrm{c}} \sec\left(\xi^{\mathcal{R},\mathcal{D}_i}\right)\right), \quad (3)$$

where H_{c} is the cloud's vertical extent, and $\xi^{\mathcal{R},\mathcal{D}_i}$ is the $\mathcal{R}$-$\mathcal{D}_i$ zenith angle. Additionally, ζ_i is the attenuation coefficient, which is a function of the visibility V_i [15, (12)]. Here, $V_i = 1.002(L_{\mathrm{c},i}M_{\mathrm{c},i})^{-0.6473}$ (km), where $L_{\mathrm{c},i}$ (g/m^3) is the cloud liquid water content (CLWC), and $M_{\mathrm{c},i}$ (cm^{-3}) is the cloud droplet number concentration [26, (1)].

Regrading the atmospheric turbulence, it causes the scintillation effect, leading to signal power fluctuations at the receiver's detector. Its PDF is characterized by the Fisher-Snedecor $\mathcal{F}$ distribution expressed as [27, (6)]

$$f_{h_{\mathrm{a}}^{\mathcal{R},\mathcal{D}_i}}\left(h_{\mathrm{a}}^{\mathcal{R},\mathcal{D}_i}\right) = \frac{a^a(b-1)^b\left(h_{\mathrm{a}}^{\mathcal{R},\mathcal{D}_i}\right)^{a-1}}{\mathcal{B}(a,b)\left(ah_{\mathrm{a}}^{\mathcal{R},\mathcal{D}_i}+b-1\right)^{a+b}}, \quad (4)$$

where $\mathcal{B}(\cdot,\cdot)$ is the beta function, while parameters a and b are given as [28, (2)]

$$a = \frac{1}{\exp(\sigma_{\ln\mathcal{S}}^2)-1}, \quad b = \frac{1}{\exp(\sigma_{\ln\mathcal{L}}^2)-1}+2, \quad (5)$$

where $\sigma_{\ln\mathcal{S}}^2$ and $\sigma_{\ln\mathcal{L}}^2$ are the small-scale and large-scale log-irradiance variances, respectively. For vertical FSO links, $\sigma_{\ln\mathcal{S}}^2$ and $\sigma_{\ln\mathcal{L}}^2$ found in [29, (47), Chapter 12] are determined by the Rytov variance, which is a function of the ground-level turbulence $C_n^2(0)$ and the rms wind speed w_{wind} [29, (38), Chapter 12].

For the pointing error, the misalignment model between HAP and UAV can be found in [15, Section III-B.3], where the PDF of $h_{\mathrm{p}}^{\mathcal{R},\mathcal{D}_i}$ is given as [15, (17)]

$$f_{h_{\mathrm{p}}^{\mathcal{R},\mathcal{D}_i}}\left(h_{\mathrm{p}}^{\mathcal{R},\mathcal{D}_i}\right) = \frac{\varphi_{\mathrm{D},i}^2}{A_{\mathrm{D}_i}^{\varphi_{\mathrm{D},i}^2}}\left(h_{\mathrm{p}}^{\mathcal{R},\mathcal{D}_i}\right)^{\varphi_{\mathrm{D},i}^2-1}, \quad 0 \le h_{\mathrm{p}}^{\mathcal{R},\mathcal{D}_i} \le A_{\mathrm{D}_i}, \quad (6)$$

TABLE 4. List of notations used in (7), (8), and (9).

Not.	Equation
C_0	$\frac{\varphi_{\mathrm{D},i}^2}{2\Gamma(a)\Gamma(b)}$
C_1	$\frac{a\varphi_{\mathrm{D},i}^2}{(b-1)\left(1+\varphi_{\mathrm{D},i}^2\right)\sqrt{\bar{\gamma}^{\mathcal{R},\mathcal{D}_i}}}$
C_2	$\frac{\varphi_{\mathrm{D},i}^2}{\Gamma(a)\Gamma(b)\pi^{3/2}}$
E_1	$\exp\left(-\frac{\hat{\gamma}}{2\bar{\hat{\gamma}}\sigma_{\mathrm{CSI},i}^2\left(1-\rho_{\mathrm{CSI},i}^2\right)}\right)$
G_{1t}	$G_{3,4}^{4,5}\left[\frac{(b-1)^2\left(h_{\mathrm{c}}^{\mathcal{R},\mathcal{D}_i}\right)^2 A_{\mathrm{D}_i}^2\rho_{\mathrm{CSI},i}^2}{2a^2\sigma_{\mathrm{CSI},i}^2\left(1-\rho_{\mathrm{CSI},i}^2\right)}\middle\vert\begin{matrix}\frac{1-a}{2},\frac{2-a}{2},\frac{1-\varphi_{\mathrm{D},i}^2}{2},\frac{2-\varphi_{\mathrm{D},i}^2}{2}\\ \frac{t}{2},\frac{b}{2},\frac{1+b}{2},-\frac{\varphi_{\mathrm{D},i}^2}{2},\frac{1-\varphi_{\mathrm{D},i}^2}{2}\end{matrix}\right]$
G_{2t}	$G_{1,2}^{1,1}\left[\frac{\hat{\gamma}}{2\bar{\hat{\gamma}}\sigma_{\mathrm{CSI},i}^2\left(1-\rho_{\mathrm{CSI},i}^2\right)}\middle\vert\begin{matrix}1\\ \frac{t+1}{2},0\end{matrix}\right]$
Z_0	$C_2\sum_{t=0}^{\infty}\frac{2^{t+a+b-4}G_{1t}}{t!\sigma_{\mathrm{CSI},i}^t}\Gamma\left(\frac{t+1}{2}\right)$

where $\varphi_{\mathrm{D},i} = \frac{\omega_{L,e(\mathrm{eq})}^{\mathcal{R},\mathcal{D}_i}}{2\sigma_{\mathrm{D},i}}$ is the ratio between the equivalent beam waist, $\omega_{L,e(\mathrm{eq})}^{\mathcal{R},\mathcal{D}_i}$, and jitter standard variance, $\sigma_{\mathrm{D},i}$.

Composite $\mathcal{R}$-$\mathcal{D}_i$ Statistical Model: the composite $\mathcal{R}$-$\mathcal{D}_i$ channel coefficient is formulated as $h^{\mathcal{R},\mathcal{D}_i} = h_{\mathrm{c}}^{\mathcal{R},\mathcal{D}_i}h_{\mathrm{a}}^{\mathcal{R},\mathcal{D}_i}h_{\mathrm{p}}^{\mathcal{R},\mathcal{D}_i}$. Given $h^{\mathcal{R},\mathcal{D}_i}$, the PDF of channel SNR is then given as [30, (12)]

$$f_{\gamma^{\mathcal{R},\mathcal{D}_i}}(\gamma) = C_0\gamma^{-1}G_{2,2}^{2,1}\left[C_1\gamma\middle\vert\begin{matrix}1-b,1+\varphi_{\mathrm{D},i}^2\\ a,\varphi_{\mathrm{D},i}^2\end{matrix}\right], \quad (7)$$

where C_0 and C_1 are given in Table 4, $\varphi_{\mathrm{D},i}$ is found in (6), and $G_{:,:}^{:,:}[\cdot]$ is the Meijer's G-function. Here, $\bar{\gamma}^{\mathcal{R},\mathcal{D}_i}$ is the average SNR computed as $\bar{\gamma}^{\mathcal{R},\mathcal{D}_i} = \frac{\Re_{\mathrm{D}}^2 P_{\mathrm{R}}^2}{\left(\sigma_n^{\mathcal{R},\mathcal{D}_i}\right)^2}\mathbb{E}\left[(h^{\mathcal{R},\mathcal{D}_i})^2\right]$, where $\mathbb{E}[\cdot]$ is the expectation operator, and $\mathbb{E}\left[(h^{\mathcal{R},\mathcal{D}_i})^2\right]$ is found in [30, (14)]. Additionally, $\Re_{\mathrm{D}}$ is the UAV's detector responsivity, P_{R} is the HAP's transmitted power, and $\sigma_n^{\mathcal{R},\mathcal{D}_i}$ is the receiver noise variance.

In practical FSO systems, the perfect CSI is not always possible due to the channel estimation error. The imprecise composite channel coefficient is expressed as [28, (10)] $\hat{h}^{\mathcal{R},\mathcal{D}_i} = \rho_{\mathrm{CSI},i}h^{\mathcal{R},\mathcal{D}_i} + \sqrt{1-\rho_{\mathrm{CSI},i}^2}\epsilon$, where $\rho_{\mathrm{CSI},i} \in [0,1]$ is correlation coefficient with $\rho_{\mathrm{CSI},i} = 1$ means no estimation errors, and $\epsilon \sim \mathcal{N}(0, \sigma_{\mathrm{CSI},i}^2)$ is the estimation error. Given $\hat{h}^{\mathcal{R},\mathcal{D}_i}$, we can determine $\bar{\hat{\gamma}}^{\mathcal{R},\mathcal{D}_i} = \frac{\Re_{\mathrm{D}}^2 P_{\mathrm{R}}^2}{\left(\sigma_n^{\mathcal{R},\mathcal{D}_i}\right)^2}\mathbb{E}\left[(\hat{h}^{\mathcal{R},\mathcal{D}_i})^2\right]$. Using the same approach in [28], we can obtain the PDF and CDF of received SNR, $\hat{\gamma}^{\mathcal{R},\mathcal{D}_i}$, in case of imperfect CSI, i.e.,

$$f_{\hat{\gamma}^{\mathcal{R},\mathcal{D}_i}}(\hat{\gamma}) = \begin{cases} C_2E_1\sum_{t=0}^{\infty}\frac{2^{0.5t+a+b-4.5}G_{1t}\hat{\gamma}^{\frac{t-1}{2}}\bar{\hat{\gamma}}^{-\frac{t+1}{2}}}{t!\left(1-\rho_{\mathrm{CSI},i}^2\right)^{(t+1)/2}\sigma_{\mathrm{CSI},i}^{2t+1}}, & \hat{\gamma} > 0,\\ 1-Z_0, & \hat{\gamma} = 0,\end{cases} \quad (8)$$

$$F_{\hat{\gamma}^{\mathcal{R},\mathcal{D}_i}}(\hat{\gamma})$$

$$= \begin{cases} C_2 \sum_{t=0}^{\infty} \frac{2^{t+a+b-4} G_{1t} G_{2t}}{t! \sigma_{\text{CSI},i}^t}, & \hat{\gamma} > 0, \\ 1 - Z_0, & \hat{\gamma} = 0, \end{cases} \tag{9}$$

where C_2, E_1, G_{1t}, G_{2t}, and Z_0 can be found in Table 4.

III. PROPOSAL OF C-HARQ WITH FRAME ALLOCATION

The proposed C-HARQ-based FAM includes two phases: $\mathcal{S}-\mathcal{R}$ and $\mathcal{R}-\mathcal{D}_i$ (re)transmissions. Notably, we employ the Reed Solomon (RS) code using a high code rate for the $\mathcal{S}-\mathcal{R}$ as the impact of weather and atmospheric turbulence are negligible on this link. In addition, it is more challenging to maintain the reliable FSO connection on the $\mathcal{R}-\mathcal{D}_i$ link under the severe impact of weather and atmospheric conditions [20]. As a result, we consider a more robust link-layer solution, i.e., incremental redundancy (IR) HARQ combining the selective repeat (SR)-ARQ and the RS code, for the $\mathcal{R}-\mathcal{D}_i$ link [21]. Here, the persistent level for both phases is set to N_t, where a data frame is clarified to be lost after $N_\text{t}+1$ (re)transmission attempts.

For the detail of our design proposal, we first describe FAM, which involves the frame allocation for multiple UAVs. Then, the operation of the C-HARQ-based FAM is presented.

A. FRAME ALLOCATION MECHANISM (FAM)

The objective of FAM is to effectively allocate the data frames for each transmission cycle while ensuring latency fairness among multiple UAVs. It consists of three major steps:

- **Step 1**: *Transmission Mode Selection for $\mathcal{D}$ Nodes*

To facilitate the frame allocation, we employ the rate adaptation scheme [10]. In other words, the number of frames allocated to each UAV is determined by its data rate, which varies depending on the channel conditions. Particularly, we use K_i transmission modes for the $\mathcal{D}_i$ node corresponding to K_i+1 ranges of SNR thresholds. By setting $\gamma_1^{\mathcal{R},\mathcal{D}_i}=0$ and $\gamma_{K_i+1}^{\mathcal{R},\mathcal{D}_i}=\infty$, other SNR thresholds, denoted as $\left\{\gamma_{k_i}^{R,Di}\right\}_{k_i=2}^{K_i}$, can be expressed by [10, (28)]

$$\gamma_{k_i}^{\mathcal{R},\mathcal{D}i} = \frac{2}{3}(2^{k_i}-1)\ln\left(\frac{1}{5\text{BER}_i}\right), \tag{10}$$

where BER_i is the targeted BER of the $\mathcal{D}_i$ node. Given the symbol rate of R_s, data bit rate on the $\mathcal{R}$-$\mathcal{D}_i$ link is given as

$$R_{i,k_i} = \begin{cases} k_i R_\text{s}, & \gamma^{\mathcal{R},\mathcal{D}_i} \in \left[\gamma_{k_i}^{\mathcal{R},\mathcal{D}_i}, \gamma_{k_i+1}^{\mathcal{R},\mathcal{D}_i}\right), \\ 0, & \gamma^{\mathcal{R},\mathcal{D}_i} < \gamma_1^{\mathcal{R},\mathcal{D}_i}. \end{cases} \tag{11}$$

- **Step 2**: *Frame Allocation for $\mathcal{D}$ Nodes*

The number of data frames allocated to each $\mathcal{D}_i$ node should satisfy the latency fairness constraint.

Definition 1: The condition for latency fairness among N UAVs can be expressed as $\tau_1=\tau_2=\cdots=\tau_N$, where τ_i is the round trip delay (RTD) of the $\mathcal{D}_i$ node.

Here, $\tau_i = 2\, t_\text{prop}^{\mathcal{S},\mathcal{R}} + t_\text{trans}^{\mathcal{S},\mathcal{R}} + 2t_\text{prop}^{\mathcal{R},\mathcal{D}_i} + t_\text{trans}^{\mathcal{R},\mathcal{D}_i}$, where $t_\text{prop}^{\mathcal{X}-\mathcal{Y}}$ and $t_\text{trans}^{\mathcal{X}-\mathcal{Y}}$ are the propagation and transmission delays on the $\mathcal{X}-\mathcal{Y}$ link, respectively.

TABLE 5. An example of FAM with R_s = 400 Mbps and n_f = 1000 frames.

UAV-1 ($\mathcal{D}_1$)			UAV-2 ($\mathcal{D}_2$)		
Mode	λ_{1,k_1}	δ_{1,k_1}	Mode	λ_{2,k_2}	δ_{2,k_2}
BPSK	500	1	BPSK	500	1
BPSK	250	1	8-QAM	750	3
QPSK	400	2	8-QAM	600	3
16-QAM	800	4	BPSK	200	1

Corollary 1: Given the burst size of n_f, the number of frames allocated to the $\mathcal{D}_i$ node using mode k_i, $k_i \in \{1,2,\cdots,K_i\}$, in a transmission cycle is determined as
if N is even,

$$\lambda_{i,k_i} = \begin{cases} \left\lceil \frac{n_f R_{i,k_i}}{\sum_{i=1}^N R_{i,k_i}} \right\rceil, & \text{if } i=1,\cdots,\frac{N}{2}, \\ \left\lfloor \frac{n_f R_{i,k_i}}{\sum_{i=1}^N R_{i,k_i}} \right\rfloor, & \text{if } i=\frac{N}{2+1},\cdots,N, \end{cases} \tag{12}$$

if N is odd,

$$\lambda_{i,k_i} = \begin{cases} \left\lceil \frac{n_f R_{i,k_i}}{\sum_{i=1}^N R_{i,k_i}} \right\rceil, & \text{if } i=1,\cdots,\frac{N-1}{2}, \\ \left\lfloor \frac{n_f R_{i,k_i}}{\sum_{i=1}^N R_{i,k_i}} \right\rfloor, & \text{if } i=\frac{N}{2},\cdots,N-1, \\ N-\sum_{i=1}^{N-1}\lambda_{i,k_i}, & \text{if } i=N, \end{cases} \tag{13}$$

where $\lceil\cdot\rceil$ and $\lfloor\cdot\rfloor$ denote the ceil and floor operators.

proof: Since $t_\text{prop}^{\mathcal{R},\mathcal{D}_1} \approx t_\text{prop}^{\mathcal{R},\mathcal{D}_2} \approx \cdots \approx t_\text{prop}^{\mathcal{R},\mathcal{D}_N}$, then $\tau_1 \approx \tau_2 \approx \cdots \approx \tau_N$ simplifies the fairness constraint to $t_\text{trans}^{\mathcal{R},\mathcal{D}_1} = t_\text{trans}^{\mathcal{R},\mathcal{D}_2} = \cdots = t_\text{trans}^{\mathcal{R},\mathcal{D}_N}$. This results in $\frac{\lambda_{1,k_1}}{R_{1,k_1}} = \frac{\lambda_{2,k_2}}{R_{2,k_2}} = \cdots = \frac{\lambda_{2,k_N}}{R_{2,k_N}}$ and together with $\sum_{i=1}^N \lambda_{i,k_i} = n_f$ as well as the condition of positive integer λ_{i,k_i}, solving equations completes the proof. □

- **Step 3**: *Burst Transmission with FAM*

In fact, the $\mathcal{R}$ node decodes received frames from the $\mathcal{S}$ node and forwards frame-by-frame to the $\mathcal{D}$ nodes. To guarantee the latency fairness constraint among $\mathcal{D}$ nodes, each burst is further partitioned into smaller groups for transmissions. Specifically, from step 2, each burst contains $\lambda_{1,k_1}, \lambda_{2,k_2}, \cdots, \lambda_{N,k_N}$ data frames allocated to $\mathcal{D}_1, \mathcal{D}_2, \cdots, \mathcal{D}_N$ nodes. It is then divided into $\psi = n_f / \sum_{i=1}^N \delta_{i,k_i}$ groups, in which each group consists of $\sum_{i=1}^N \delta_{i,k_i}$ frames. Here, δ_{i,k_i} is the number of frames belonging to the $\mathcal{D}_i$ node in a group, and it is determined based on the ratio of $\frac{\delta_{1,k_1}}{\lambda_{1,k_1}} = \frac{\delta_{2,k_2}}{\lambda_{2,k_2}} = \cdots = \frac{\delta_{N,k_N}}{\lambda_{N,k_N}}$. It is worth noting that the data bit rate on $\mathcal{S}$-$\mathcal{R}$ is defined as $R_b = R_\text{s} \sum_{i=1}^N \delta_{i,k_i}$ corresponding to $M-$QAM modulation with $M = 2^{\sum_{i=1}^N \delta_{i,k_i}}$.

An example of FAM is illustrated in Fig. 5 for different transmission modes when $N=2$ UAVs.

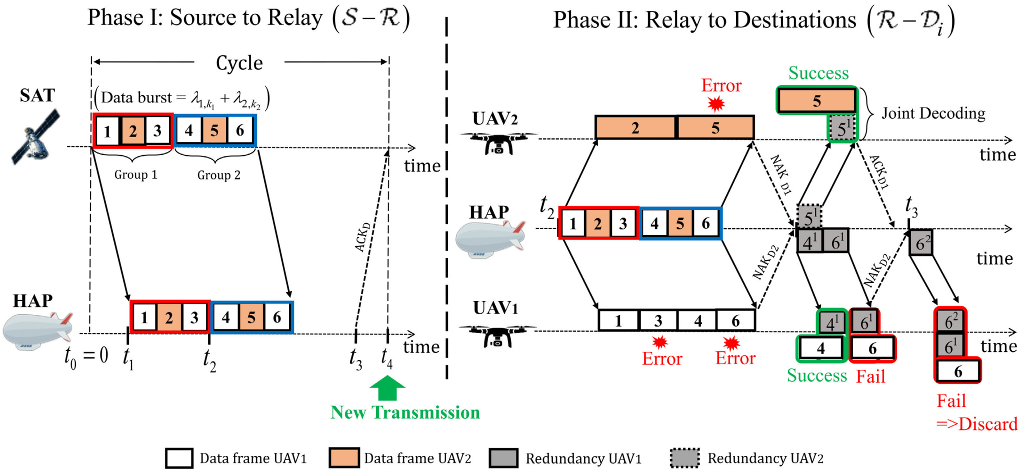

FIGURE 3. An example of the proposed link-layer C-HARQ-based FAM for multiple UAV-mounted BSs with $N = 2$ UAVs.

B. OPERATION OF C-HARQ-BASED FAM

The operation of C-HARQ-based FAM is described as follows.

- **Phase I**: *$\mathcal{S}$-to-$\mathcal{R}$ Transmissions*

Initially, the $\mathcal{S}$ node sends a fixed-sized burst containing n_f link-layer frames to the $\mathcal{R}$ node. Each link-layer frame is encoded with the RS code using a high code rate. The burst is divided into ψ frame groups for the transmissions to the $\mathcal{R}$ node, as described in step 3. Then, the $\mathcal{R}$ node decodes each received group and forwards successful frames to corresponding $\mathcal{D}$ nodes. In case of transmission failure, the $\mathcal{R}$ node discards all the frames in the whole group from the $\mathcal{S}$ node. This is to guarantee the latency fairness constraint among multiple UAVs.

- **Phase II**: *$\mathcal{R}$-to-$\mathcal{D}$ (Re)transmissions*

Each $\mathcal{D}_i$ node decodes the frames forwarded from the $\mathcal{R}$ node. If no errors are detected by the standard cyclic redundancy check (CRC), the $\mathcal{D}_i$ node sends the $\mathrm{ACK}_{\mathrm{D}_i}$ to the $\mathcal{R}$ node. Otherwise, the $\mathcal{D}_i$ node returns the $\mathrm{NAK}_{\mathrm{D}}$ feedback along with the erroneous frame's sequence number to the $\mathcal{R}$ node to request a redundancy frame. The $\mathcal{D}_i$ node then combines the newly received redundancy frames with previously received ones for joint decoding employed by the IR-HARQ scheme. The $\mathcal{R}$ node retransmits the redundancy frames until the $\mathcal{D}_i$ node successfully decodes it, or the number of attempts reaches the persistent level of N_{t} (the frame is discarded and clarified to be lost). When the $\mathcal{R}$ node receives $\mathrm{ACK}_{\mathrm{D}}$ from all $\mathcal{D}_i$ nodes (the $\mathrm{ACK}_{\mathrm{D}}$ is also returned when reaching the persistent level), it then forwards to the $\mathcal{S}$ node for a new transmission cycle.

Example: An example of the proposed C-HARQ-based FAM is illustrated in Fig 3, when $n_f = 6$ frames/burst. Also, $\lambda_{1,k_1} = 4$ frames, $\delta_{1,k_1} = 2$ frames/group, $k_1 = 1$ (for $\mathcal{D}_1$ using BPSK) and $\lambda_{2,k_2} = 2$ frames, $\delta_{1,k_1} = 1$ frame/group, $k_2 = 2$ (for $\mathcal{D}_2$ using QPSK). As for phase II, frames 4, 6 (belongs to $\mathcal{D}_1$) and frame 5 (belongs to $\mathcal{D}_2$) are assumed to be uncorrected. The additional redundancies for these frames are then retransmitted for joint decoding with previously received ones. We also observe that frame 6 is discarded as it is still uncorrected after reaching the persistent level.

IV. PERFORMANCE ANALYSIS

This section focuses on the performance analysis for the proposed scheme. Several performance metrics are analytically derived, including average throughput, average frame delay, and energy efficiency.

A. AVERAGE THROUGHPUT AND ENERGY EFFICIENCY

The average system throughput is defined as the average total number of successfully received data from all N UAVs in a cycle duration, which is computed as

$$\bar{S} = \sum_{k_1=1}^{K_1}\sum_{k_2=1}^{K_2}\cdots\sum_{k_N=1}^{K_N} \Pr_1(k_1)\Pr_2(k_2)\cdots\Pr_N(k_N) \times \frac{\left(\bar{A}_{1,k_1}+\bar{A}_{2,k_2}+\cdots+\bar{A}_{N,k_N}\right)N_f}{\bar{\tau}_{\mathrm{c}}}, \tag{14}$$

where N_f is the data frame size, K_i is the total number of transmission modes for the $\mathcal{D}_i$ node, $\bar{\tau}_{\mathrm{c}}$ is the average cycle duration analyzed in Section IV-B, and $\Pr_i(k_i)$ is the probability that the $\mathcal{D}_i$ node uses the transmission mode k_i, i.e.,

$$\Pr_i(k_i) = F_{\gamma^{\mathcal{R},\mathcal{D}_i}}(\gamma_{k_i+1}^{\mathcal{R},\mathcal{D}_i}) - F_{\gamma^{\mathcal{R},\mathcal{D}_i}}(\gamma_{k_i}^{\mathcal{R},\mathcal{D}_i}), \tag{15}$$

where $F_{\gamma^{\mathcal{R},\mathcal{D}_i}}(\cdot)$ is the channel SNR cumulative distribution function (CDF) on the $\mathcal{R}$-$\mathcal{D}_i$ link defined in Section III. Additionally, $\bar{A}_{i,k_i}$ is the average successful data frames of the $\mathcal{D}_i$ node using the mode k_i, which is calculated as

$$\bar{A}_{i,k_i} = \lambda_{i,k_i}\underbrace{\left(1-\overline{\mathrm{FER}}_{k_i}^{\mathcal{S},\mathcal{R}}\right)^{\beta}}_{\mathcal{S}-\mathcal{R}}$$

$$\times \underbrace{\sum_{z=1}^{N_t}\left[\prod_{j=1}^{z-1}\overline{\mathrm{FER}}_{k_i,j}^{\mathcal{R},\mathcal{D}_i}\left(1-\overline{\mathrm{FER}}_{k_i,z}^{\mathcal{R},\mathcal{D}_i}\right)\right]}_{\mathcal{R}-\mathcal{D}_i}, \quad (16)$$

where λ_{i,k_i} is given in (12) and (13), N_t is the HARQ's persistent level, and $\beta = \sum_{i=1}^{N}\delta_{i,k_i}$ is total number of frames in a group. Additionally, $\overline{\mathrm{FER}}_{k_i,z}^{\mathcal{X},\mathcal{Y}}$ is the average frame error rate (FER) on the $\mathcal{X}$-$\mathcal{Y}$ link (either $\mathcal{S}$-$\mathcal{R}$ or $\mathcal{R}$-$\mathcal{D}_i$) using mode k_i at z-th transmission attempt, which is given as [14, (16)]

$$\overline{\mathrm{FER}}_{k_i,z}^{\mathcal{X},\mathcal{Y}} = \sum_{j=t_z+1}^{N_f+(z-1)N_r}\binom{N_f+(z-1)N_r}{j}\left(\overline{\mathrm{P}}_{ek_i}^{\mathcal{X},\mathcal{Y}}\right)^j \times\left(1-\overline{\mathrm{P}}_{ek_i}^{\mathcal{X},\mathcal{Y}}\right)^{N_f+(z-1)N_r-j}, \quad (17)$$

where $t_z = \left\lfloor \frac{(z-1)}{2}N_r \right\rfloor$ is the RS code's error-correction capability at the z-th transmission attempt, and N_r is the redundancy size. Here, it is noted that each frame transmitted from the $\mathcal{S}$ node contains N_r redundancy bits, which is for the RS code. This allows the $\mathcal{R}$ node to correct the number of error bits in each received frame up to $\frac{N_r}{2}$ bits. Also, the transmission mode for the $\mathcal{S}$-$\mathcal{R}$ link, which corresponds to the mode k_i on the $\mathcal{R}$-$\mathcal{D}_i$ link, is defined by step 3 in section II-B. As a result, $\overline{\mathrm{FER}}_{k_i}^{\mathcal{S},\mathcal{R}}$ represents for $\overline{\mathrm{FER}}_{k_i,2}^{\mathcal{S},\mathcal{R}}$ as shown in (17). In addition, $\overline{\mathrm{P}}_{ek_i}^{\mathcal{X},\mathcal{Y}}$ is the average BER, which is computed as

$$\overline{\mathrm{P}}_{ek_i}^{\mathcal{X},\mathcal{Y}} = \frac{1}{\mathrm{Pr}_i(k_i)}\int_{\gamma_{k_i}^{\mathcal{X},\mathcal{Y}}}^{\gamma_{k_i+1}^{\mathcal{X},\mathcal{Y}}} \mathrm{P}_{ek_i}^{\mathcal{X},\mathcal{Y}}(\gamma^{\mathcal{X},\mathcal{Y}})f_\gamma(\gamma^{\mathcal{X},\mathcal{Y}})d\gamma^{\mathcal{X},\mathcal{Y}}, \quad (18)$$

where $\mathrm{P}_{ek_i}^{\mathcal{X},\mathcal{Y}}(\gamma^{\mathcal{X},\mathcal{Y}})$ is the instantaneous BER found in [10, (27)]. Here, it is worth noting that $k_i = 0$ indicates the system's outage, i.e., $\overline{\mathrm{FER}}_{0,z}^{\mathcal{X},\mathcal{Y}} = 1$.

Given $\overline{S}$ in (14), we can determine the energy efficiency. It is defined as the ratio of the average total throughput over the total system power consumption, which is given as

$$\overline{\eta}_{\mathrm{EE}} = \frac{\overline{S}}{P_{\mathrm{S}}+\sum_{i=1}^{N}P_{\mathrm{R}_i}}, \quad (19)$$

where P_{S} and P_{R_i} are the transmitted powers of satellite and HAP (for $\mathcal{R}$-$\mathcal{D}_i$ link), respectively. Here, we use the same HAP's transmitted power for each user, i.e., $P_{\mathrm{R}_1} = P_{\mathrm{R}_2} = \cdots = P_{\mathrm{R}_N} = P_{\mathrm{R}}$, or $\sum_{i=1}^{N}P_{\mathrm{R}_i} = NP_{\mathrm{R}}$.

B. FRAME DELAY ANALYSIS

To complete (14), we need to determine the average cycle duration, denoted by $\overline{\tau}_{\mathrm{c}}$. Here, it is worth noting that the $\mathcal{R}$ node forwards ACK to the $\mathcal{S}$ node for a new transmission cycle if it receives enough $\mathrm{ACK}_{\mathrm{D}_i}$ from the $\mathcal{D}_i$ node, $i \in \{1, 2, \cdots, N\}$. As a result, it is computed as

$$\overline{\tau}_{\mathrm{c}} = \sum_{k_1=1}^{K_1}\sum_{k_2=1}^{K_2}\cdots\sum_{k_N=1}^{K_N}\mathrm{Pr}_1(k_1)\mathrm{Pr}_2(k_2)\cdots\mathrm{Pr}_n(k_n) \times\max\left(\overline{\tau}_{1,k_1}, \overline{\tau}_{2,k_2}, \cdots, \overline{\tau}_{N,k_N}\right), \quad (20)$$

where $\overline{\tau}_{i,k_i}$ is the average RTD of the $\mathcal{D}_i$ node using the transmission mode k_i, which is determined as

$$\overline{\tau}_{i,k_i} = \underbrace{2t_{\mathrm{prop}}^{\mathcal{S},\mathcal{R}}+\beta\frac{N_f+N_r}{R_b}}_{\mathcal{S}-\mathcal{R}} + \underbrace{2t_{\mathrm{prop}}^{\mathcal{R},\mathcal{D}_i}+\overline{\lambda}_{i,k_i}^{\mathcal{R},\mathcal{D}_i}\frac{N_f}{R_{i,k_i}}}_{\text{Initial transmission on } \mathcal{R}-\mathcal{D}_i} + \underbrace{\sum_{z=1}^{N_t-2}\left(1-\left(1-\overline{\mathrm{FER}}_{k_i,z}^{\mathcal{R},\mathcal{D}_i}\right)^{\overline{N}_{i,z}}\right)2t_{\mathrm{prop}}^{\mathcal{R},\mathcal{D}_i}+\overline{N}_{i,z+1}\frac{N_r}{R_{i,k_i}}}_{\text{Retransmissions on } \mathcal{R}-\mathcal{D}_i}, \quad (21)$$

where β is found in (16), while N_t, N_f, N_r, R_b, $t_{\mathrm{prop}}^{\mathcal{S},\mathcal{R}}$, and $t_{\mathrm{prop}}^{\mathcal{R},\mathcal{D}_i}$ are defined in section II-B.

In addition, $\overline{N}_{i,z}$ is the average number of frames during the z^{th} transmission attempt by the $\mathcal{D}_i$ node, which is determined as

$$\overline{N}_{i,z} = \begin{cases}\overline{\lambda}_{i,k_i}^{\mathcal{R},\mathcal{D}_i}, & z=1,\\ \overline{\lambda}_{i,k_i}^{\mathcal{R},\mathcal{D}_i}\prod_{j=1}^{z-1}\overline{\mathrm{FER}}_{k_i,j}^{\mathcal{R},\mathcal{D}_i}, & z>1,\end{cases} \quad (22)$$

where $\overline{\lambda}_{i,k_i}^{\mathcal{R},\mathcal{D}_i} = \lambda_{i,k_i}\left(1-\overline{\mathrm{FER}}_{k_i}^{\mathcal{R},\mathcal{D}_i}\right)^{\beta}$ is the average number of transmission frame on the $\mathcal{R}$-$\mathcal{D}_i$ link, and $\overline{\mathrm{FER}}_{k_i,z}^{\mathcal{R},\mathcal{D}_i}$ is found in (17).

On the other hand, the average frame delay is defined as the average time duration required to deliver a frame from the $\mathcal{S}$ node until the $\mathcal{D}$ nodes decode that frame successfully. It is, then, calculated as

$$\overline{D} = \sum_{k_1=1}^{K_1}\sum_{k_2=1}^{K_2}\cdots\sum_{k_N=1}^{K_N}\mathrm{Pr}_1(k_1)\mathrm{Pr}_2(k_2)\cdots\mathrm{Pr}_N(k_N) \times\max\left(\overline{D}_{1,k_1}, \overline{D}_{2,k_2}, \cdots, \overline{D}_{N,k_N}\right), \quad (23)$$

where $\overline{D}_{i,k_i}$ is the time duration required to successfully deliver a data frame for the $\mathcal{D}_i$ node, in which the transmission mode k_i is used on the $\mathcal{R}$-$\mathcal{D}_i$ link. It is determined as

$$\overline{D}_{i,k_i} = \overline{\tau}_{i,k_i} - \frac{(\overline{\lambda}_{i,k_i}^{\mathcal{R},\mathcal{D}_i}-1)N_f}{2R_{i,k_i}}, \quad (24)$$

where $\overline{\tau}_{i,k_i}$ is given in (21).

V. NUMERICALS RESULT AND DISCUSSIONS

This section presents and discusses the performance of the proposed C-HARQ-based FAM/rate adaptation in terms of total throughput, average frame delay, and energy efficiency. The effectiveness of the proposed design is also highlighted by comparing its performance with the conventional C-HARQ without FAM approaches [14], [15]. Monte Carlo simulations, conducted with a discrete-event simulator, are also performed to verify all the analytical derivations.

TABLE 6. Simulation setting for different links.

Name	Symbol	Value
UAV 1: Parameters for $\mathcal{R}$-$\mathcal{D}_1$ Link		
Ground-level turbulence	$C_n^2(0)$	10^{-14} $\mathrm{m}^{-2/3}$
Zenith angle	$\xi^{\mathcal{R},\mathcal{D}_1}$	$40°$
Targeted BER (QoS)	BER_1	10^{-3}
HAP's Jitter angle	$\theta_{\mathrm{Rs},1}$	50 μrad
UAV 2: Parameters for $\mathcal{R}$-$\mathcal{D}_2$ Link		
Ground-level turbulence	$C_n^2(0)$	10^{-13} $\mathrm{m}^{-2/3}$
Zenith angle	$\xi^{\mathcal{R},\mathcal{D}_2}$	$50°$
Targeted BER (QoS)	BER_2	10^{-5}
HAP's Jitter angle	$\theta_{\mathrm{Rs},2}$	70 μrad

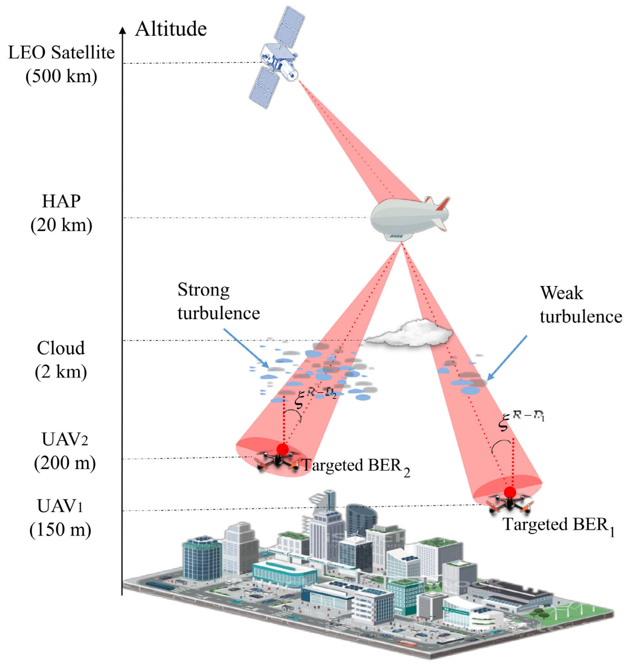

FIGURE 4. An illustrative scenario with $N = 2$ UAVs considered for simulations.

A. PARAMETER SETTINGS

For the sake of demonstration, we consider $N = 2$ UAVs[1] suffering different turbulence channel conditions as illustrated in Fig. 4, in which parameters for different links are given in Table 6. For the rate adaptation scheme, we use the symbol rate of $R_s = 500$ Msps with $K_1 = K_2 = 4$ transmission modes, i.e., BPSK, QPSK, 8-QAM, and 16-QAM. Unless otherwise noted, the parameters used in the analysis are as follows.

- *The $\mathcal{S}$ node (LEO satellite)*: altitude $H_{\mathrm{S}} = 500$ km, optical wavelength $\lambda_{\mathrm{opt}} = 1550$ nm, zenith angle $\xi^{\mathcal{S},\mathcal{R}} = 30°$, divergence angle $\theta_{\mathrm{d}}^{\mathcal{S}} = 10$ μrad, jitter angle $\theta_{\mathrm{Sx}} = \theta_{\mathrm{Sy}} = 0.3$ μrad, transmitted power $P_{\mathrm{S}} = 25$ dBm, and a collimated Gaussian beam ($F_0 = \infty$).
- *The $\mathcal{R}$ node (HAP)*: altitude $H_{\mathrm{R}} = 20$ km, transmitted power $P_{\mathrm{R}_1} = P_{\mathrm{R}_2} = P_{\mathrm{R}} = 20$ dBm, aperture diameter $D_{\mathrm{r}} = 10$ cm, detector responsivity $\Re_{\mathrm{R}} = 0.9$, noise standard deviation $\sigma_n^{\mathcal{S},\mathcal{R}} = 10^{-7}$ A/Hz, divergence angle $\theta_{\mathrm{d},1}^{\mathcal{R}} = \theta_{\mathrm{d},2}^{\mathcal{R}} = 1$ mrad, $\mu_{\mathrm{Rx}} = \mu_{\mathrm{Ry}} = 0$, and $\sigma_{\mathrm{Rx}} = \sigma_{\mathrm{Ry}} = 1$ m, and collimated Gaussian beams ($F_0 = \infty$).
- *The $\mathcal{D}$ nodes (UAVs)*: altitudes $H_{\mathrm{D}_1} = 150$ m and $H_{\mathrm{D}_2} = 200$ m, detector responsivity $\Re_{\mathrm{D}_1} = \Re_{\mathrm{D}_2} = 0.9$, aperture diameter $D_{\mathrm{D}_1} = D_{\mathrm{D}_2} = 10$ cm, noise standard deviation $\sigma_n^{\mathcal{R},\mathcal{D}_1} = \sigma_n^{\mathcal{R},\mathcal{D}_2} = 10^{-7}$ A/Hz, initial position $(\mu_{\mathrm{Ux},i}, \mu_{\mathrm{Uy},i}) = 0$, and standard deviation of UAV position $(\sigma_{\mathrm{Ux},i}, \sigma_{\mathrm{Uy},i}) = 1$ m.
- *C-HARQ and other parameters*: data frame size $N_f = 975$ bytes, redundancy size $N_r = 24$ bytes, burst size $n_f = 2520$ frames, and persistent level $N_{\mathrm{t}} = 3$. In addition, rms wind speed $w_{\mathrm{wind}} = 21$ m/s, vertical extent of clouds $H_{\mathrm{c}} = 2$ km, number cloud droplet concentration $M_{\mathrm{c},1} = M_{\mathrm{c},2} = 200$ cm^{-3}, CLWC values of $L_{\mathrm{c},1} = L_{\mathrm{c},2} = 1$ $\mathrm{mg/m}^3$, and $\rho_{\mathrm{CSI},i} = 1$.

B. PERFORMANCE EVALUATION

First, we quantitatively highlight the effectiveness of the proposed C-HARQ-based FAM by comparing its throughput performance with the conventional C-HARQ without FAM [14], [15]. Particularly, Figs. 5 (a), (b), and (c) analyze the average total throughput for different channel conditions of the $\mathcal{R}$-$\mathcal{D}_2$ FSO link. Also, different HAP's transmitted powers are taken into account. As is expected, our proposed C-HARQ-based FAM achieves a significant total throughput enhancement compared to the conventional approach over various channel conditions of the $\mathcal{R}$-$\mathcal{D}_2$ link, i.e., (a) UAV's positions compared to the center of HAP's beam footprint, (b) CLWC values, and (c) HAP's zenith angles. It is because more data frames are allocated to the UAV with good channel conditions and vice versa. This confirms the effectiveness of the frame allocation for multiple UAVs experiencing different channel conditions. On the other hand, using Fig. 5 (a), we can determine the operational area of the UAV $\mathcal{D}_2$ to retain a targeted total throughput performance for our proposed scheme. For instance, to achieve a total throughput of above 2 Gbps, the UAV $\mathcal{D}_2$ should operate within 10 m from the center of HAP's beam footprint. Also, as seen from all figures, the analytical results closely follow simulated ones, which validates the correctness of the model and analysis.

Next, we focus on the selection of HAP's transmitted power by considering the performance tradeoff for various applications. Figure 6 investigates the performance tradeoff, i.e., (a) energy efficiency/throughput, (b) last-mile frame delay/throughput, and (c) energy efficiency/average frame delay, for different targeted BERs on the $\mathcal{R}$-$\mathcal{D}_1$ link. Using these figures, we can further highlight the outperformance of our proposed design compared to the conventional C-HARQ without FAM in terms of not only total throughput but also the energy efficiency and average frame delay. Specifically,

[1] It is worth noting that we select $N = 2$ UAVs for simulations to highlight the proposed C-HARQ-based FAM. Additionally, a generalized number of UAVs can be considered [31], which is possible by using our provided analytical framework. Moreover, the trajectory of UAV-mounted BSs [32], [33] would be investigated in our future work.

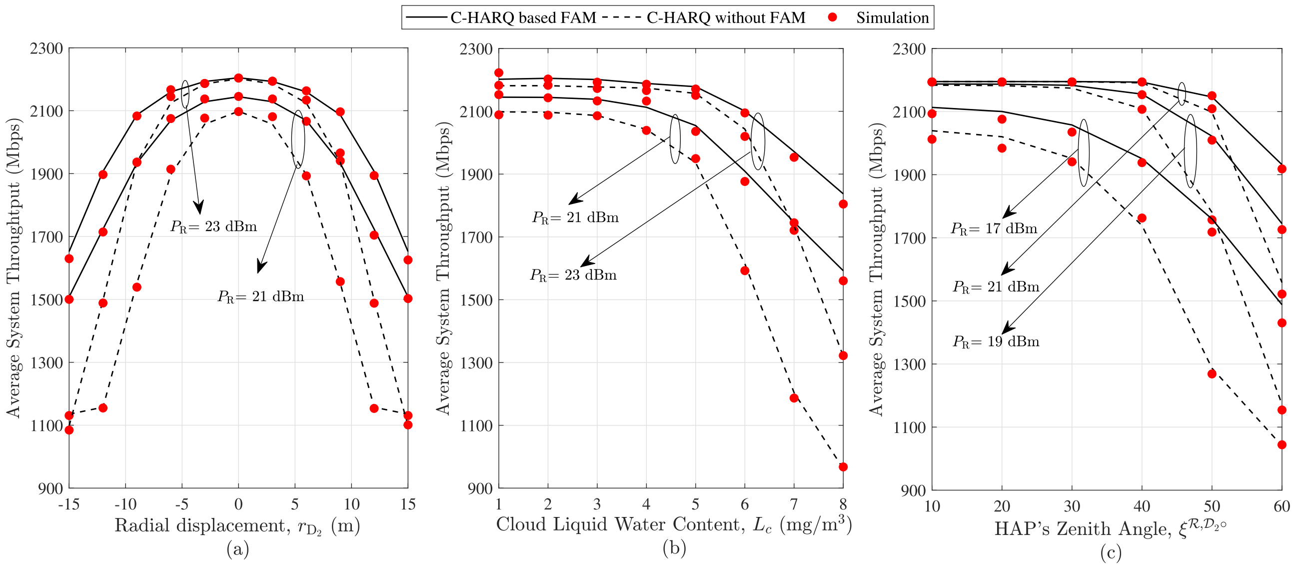

FIGURE 5. Throughput performance comparison for various channel conditions on $\mathcal{R}$-$\mathcal{D}_2$ FSO link.

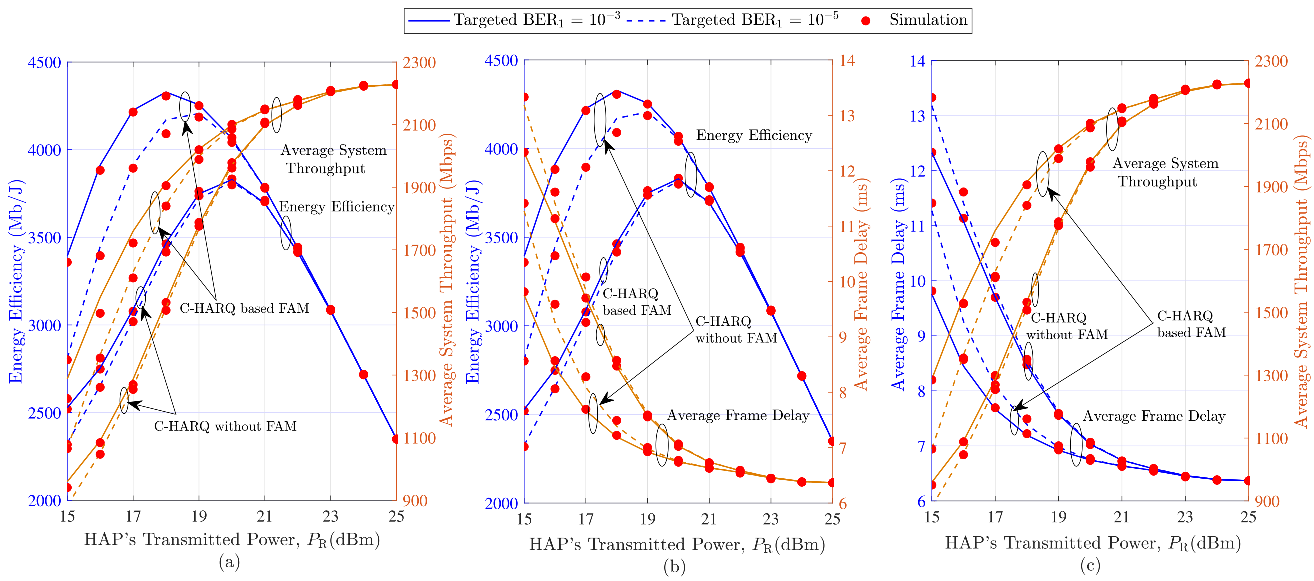

FIGURE 6. Throughput, delay, and energy efficiency performance tradeoff for different targeted BERs on $\mathcal{R}$-$\mathcal{D}_1$ FSO link.

Fig. 6 (a) analyzes the tradeoff between system throughput and energy efficiency over a range of HAP's transmitted powers. As seen, we can achieve higher throughput and energy efficiency levels with higher targeted BER values as we have more chances to select higher transmission modes with higher data rates. Also, from this figure, there exists an optimal value of transmitted power, at which the energy efficiency is maximized. It is because when the HAP's transmitted power becomes high enough, the frame error rate saturates, and any further increases of P_R only result in additional energy consumption. However, this optimal power level is not always the optimal one for the throughput performance. For example, when the targeted BER$_1$ $= 10^{-3}$, the HAP's transmitted power for each UAV should be 18 dBm to maximize the energy efficiency while retaining a total throughput level of 1.9 Gbps. A similar observation for the tradeoff between energy efficiency and average frame delay is illustrated in Fig. 6 (b). The optimal HAP transmitted power of 18 dBm for the maximum energy efficiency corresponds to the frame delay level of 7 ms. In addition, we further investigate the tradeoff between average frame delay and total throughput performance in Fig. 6 (c). Using this figure, for instance, we can decide the HAP's transmitted power for each UAV of 20 dBm to maintain the total achievable throughput above 2 Gbps and the average frame delay below 7 ms, when the targeted BER$_1$ $= 10^{-3}$.

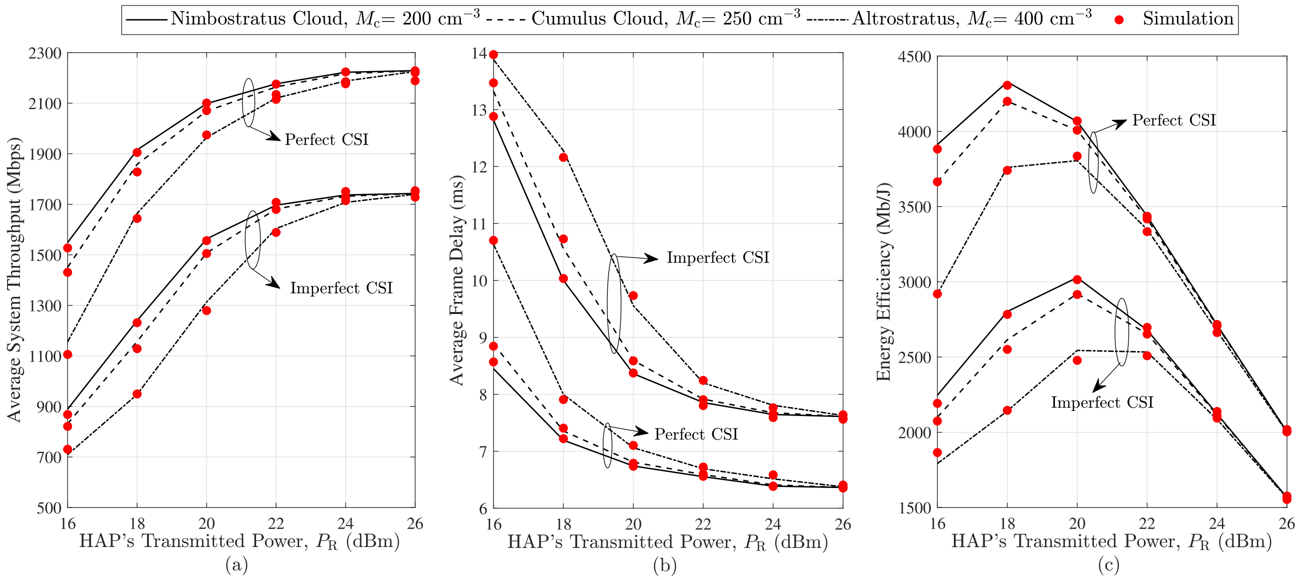

FIGURE 7. **Throughput, delay, and energy efficiency performance of the proposed scheme for different CSI conditions.**

A critical issue on the performance of FSO-based aerospace backhaul networks using C-HARQ-based FAM is the severe impact of imperfect CSI. Here, we consider the imperfect CSI due to the channel estimation errors at UAV-based receivers. Figures 7 (a), (b), (c) analyze the impact of imperfect CSI on the throughput, average frame delay, and energy efficiency performance over a range of HAP's transmitted powers, respectively. Also, we consider $\rho_{\mathrm{CSI},1} = \rho_{\mathrm{CSI},2} = 1$ (for the perfect CSI condition) and $\rho_{\mathrm{CSI},1} = 0.8$, $\rho_{\mathrm{CSI},2} = 1$ (for the imperfect CSI condition). Additionally, different cloud types, i.e., Nimbostratus ($M_c = 200$ cm^{-3}), Cumulus ($M_c = 250$ cm^{-3}), and Alstrostratus ($M_c = 400$ cm^{-3}), are taken into account. As is evident, imperfect CSIs result in significant performance deterioration, including throughput, average frame delay, and energy efficiency. For example, from Fig. 7 (a), when $M_c = 200$ cm^{-3} and $P_R = 24$ dBm, the maximum achievable total throughput levels are 1.75 Gbps and 2.25 Gbps for imperfect and perfect CSI conditions, respectively. Also, as depicted in Fig. 7 (b), the minimum delay levels for corresponding imperfect and perfect CSI conditions are 7.5 ms and 6.5 ms. In addition, as illustrated in Fig. 7 (c), the HAP's transmitted powers required to reach the optimal energy efficiency performance are 20 dBm and 18 dBm for respectively the imperfect and perfect CSI conditions.

We now investigate the impact of FSO-based $\mathcal{S}$-$\mathcal{R}$ link to the system performance. While the $\mathcal{S}$-$\mathcal{R}$ link can be reliable when using RS code, it is necessary to investigate the system performance without RS code. An essential issue in designing optical satellite systems is the proper selection of SAT's transmitted power. For this purpose, we plot in Fig. 8 (b) the total throughput performance within a satellite pass duration defined by a range of zenith angles in Fig. 8 (a). Also, different satellite's transmitted power values are considered.

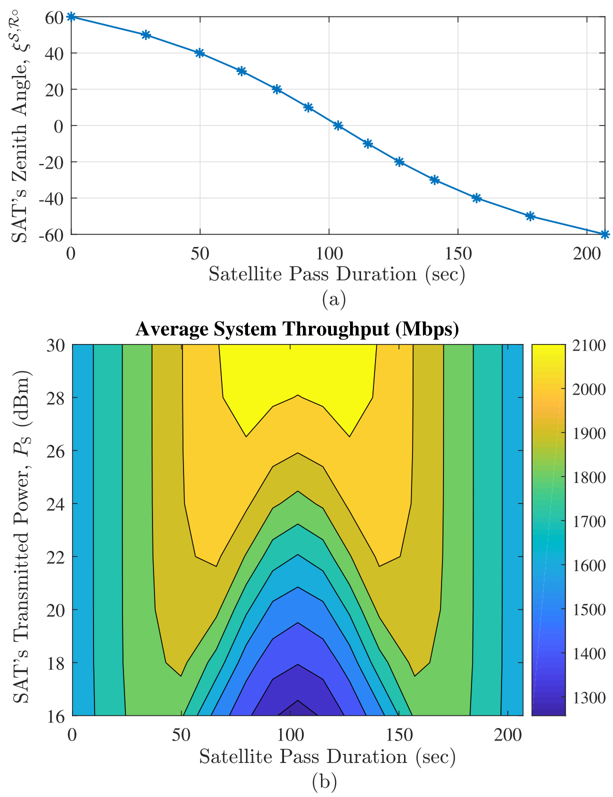

FIGURE 8. **Throughput performance over an LEO satellite pass for different SAT's transmitted powers.**

Using this figure, we can determine the transmitted power to achieve a targeted throughput level over a satellite pass duration. For example, the transmitted power should be chosen as 25 dBm to maintain a targeted total throughput level above 1.9 Gbps during the satellite pass duration.

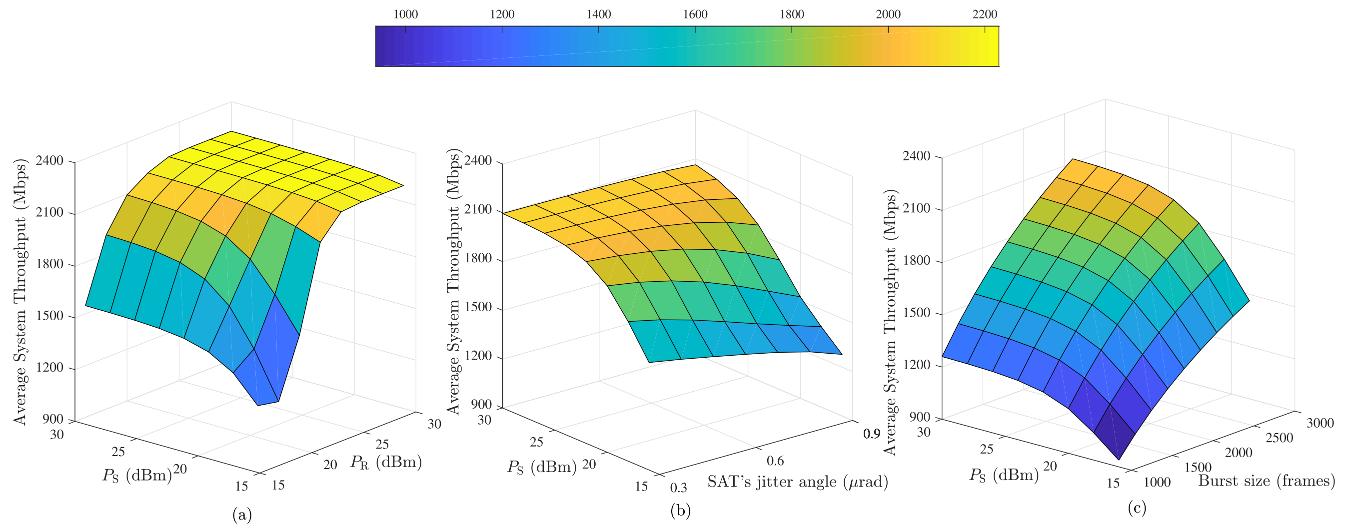

FIGURE 9. Throughput performance versus SAT's transmitted power for different (a) HAP's transmitted powers, (b) SAT's pointing error conditions, and (c) burst size values.

Finally, Fig. 9 analyzes the throughput performance over a range of satellite's transmitted power for different (a) HAP's transmitted power levels, (b) pointing misalignment conditions indicated by the SAT's jitter angles, and (c) the burst size values. Specifically, from Fig. 9 (a), given the HAP's power level, we can determine the satellite's transmitted power to reach the maximum total throughput performance. For example, when $P_R = 22$ dBm, we can select the satellite's transmitted power of 24 dBm to maintain the maximum total throughput level of 2.2 Gbps. In addition, as shown in Fig. 9 (b), the pointing misalignment indicated by the satellite's jitter angle considerably deteriorates the throughput performance. Using this figure, for instance, when $\theta_{Sx} = \theta_{Sx} = 0.5\mu$rad, we can decide the satellite's transmitted power level of 26 dBm to reach the maximum achievable total throughput of 2.1 Gbps. On the other hand, using Fig. 9 (c), we can choose the satellite power level corresponding to a burst size value to achieve the maximum throughput level. When the burst size $n_f = 2200$ frames, we can use the satellite's transmitted power of 24 dBm to retain a maximum achievable total throughput level of 1.9 Gbps.

C. DESIGN GUIDELINES

Based on the insightful numerical results obtained, we provide a design guideline that is highly recommended for effectively implementing our proposed design in practice, as follows.

- Given $P_R = 21$ dBm, the operational area of UAV $\mathcal{D}_2$ should be within 10 m from the center of HAP's beam footprint to maintain the targeted total throughput level above 2 Gbps.
- There is a tradeoff between throughput and energy efficiency. In other words, an optimal value of HAP's transmitted power to maximize energy efficiency is not always the optimal one for the throughput and delay performance. When the targeted $\text{BER}_1 = 10^{-3}$, we can select $P_R = 18$ dBm to optimize the energy efficiency while retaining a total throughput level of 1.9 Gbps and delay level of 7 ms.
- In the presence of the Nimbostratus clouds with $M_c = 200\text{cm}^{-3}$, when $P_R = 24$ dBm, the maximum achievable total throughput levels are 1.75 Gbps and 2.25 Gbps for imperfect and perfect CSI conditions, respectively. The minimum delay levels for corresponding imperfect and perfect CSI conditions are also 7.5 ms and 6.5 ms.
- We can decide $P_S = 25$ dBm to retain a targeted total throughput level above 1.9 Gbps during the satellite pass duration.
- When $P_R = 22$ dBm, we can select $P_S = 24$ dBm to maintain the maximum total throughput level of 2.2 Gbps.
- For the satellite's pointing misalignment condition of $\theta_{Sx} = \theta_{Sx} = 0.5\mu$rad, we can decide $P_S = 26$ dBm to reach the maximum achievable total throughput of 2.1 Gbps.
- When the burst size $n_f = 2200$ frames, we can use $P_S = 24$ dBm to retain a maximum achievable total throughput level of 1.9 Gbps.

VI. CONCLUSION

This paper presented a novel design of C-HARQ-based FAM/rate adaptation for reliable FSO-based aerospace backhaul networks supporting multiple UAV-mounted BSs. The idea of FAM was to efficiently allocate data frames while guaranteeing latency fairness constraints among multiple UAVs that suffer varying turbulence channel conditions with QoS requirements. The rate adaptation scheme was also used to facilitate the C-HARQ-based FAM operation. Furthermore, we developed a comprehensive analytical framework taking into account the channel models for

LEO satellite-HAP/HAP-UAV links and imperfect CSI. The analytical frameworks allowed for the assessment of performance metrics, including total throughput, average frame delay, and energy efficiency. Numerical results highlighted the effectiveness of our proposed scheme by comparing it with the conventional approach without FAM for various turbulence channel conditions and QoS requirements. The obtained results also demonstrated the severe impact of imperfect CSI due to channel estimation errors on the system performance. In addition, we provided the design guidelines that could be helpful for the practical design of FSO-based aerospace backhaul networks. Monte Carlo simulation was conducted to verify the theoretical analysis, and the results demonstrated a remarkable agreement between the analytical and simulated ones. Future work would be interesting to incorporate the impact of access networks, in which the design of C-HARQ-based FAM should consider distributed required traffic from different ground users with diverse QoS demands and user densities.

REFERENCES

[1] G. M. Karam, M. Gruber, I. Adam, F. Boutigny, Y. Miche, and S. Mukherjee, "The evolution of networks and management in a 6G world: An inventor's view," *IEEE Trans. Netw. Service Manage.*, vol. 19, no. 4, pp. 5395–5407, Dec. 2022.

[2] D. Zhou, M. Sheng, J. Li, and Z. Han, "Aerospace integrated networks innovation for empowering 6G: A survey and future challenges," *IEEE Commun. Surveys Tuts.*, vol. 25, no. 2, pp. 975–1019, 2nd Quart., 2023.

[3] Z. Jia, M. Sheng, J. Li, D. Zhou, and Z. Han, "Joint HAP access and LEO satellite backhaul in 6G: Matching game-based approaches," *IEEE J. Sel. Areas Commun.*, vol. 39, no. 4, pp. 1147–1159, Apr. 2021.

[4] Y. Zhu, W. Bai, M. Sheng, J. Li, D. Zhou, and Z. Han, "Joint UAV access and GEO satellite backhaul in IoRT networks: Performance analysis and optimization," *IEEE Internet Things J.*, vol. 8, no. 9, pp. 7126–7139, May 2021.

[5] Z. Gu, J. Zhang, Y. Ji, L. Bai, and X. Sun, "Network topology reconfiguration for FSO-based fronthaul/backhaul in 5G+ wireless networks," *IEEE Access*, vol. 6, pp. 69426–69437, 2018.

[6] Y. Dong, M. Z. Hassan, J. Cheng, M. J. Hossain, and V. C. M. Leung, "An edge computing empowered radio access network with UAV-mounted FSO fronthaul and backhaul: Key challenges and approaches," *IEEE Wireless Commun.*, vol. 25, no. 3, pp. 154–160, Jun. 2018.

[7] J.-H. Lee, K.-H. Park, Y.-C. Ko, and M.-S. Alouini, "Spectral-efficient network design for high-altitude platform station networks with mixed RF/FSO system," *IEEE Trans. Wireless Commun.*, vol. 21, no. 9, pp. 7072–7087, Sep. 2022.

[8] Y. Zhou, Z. Gu, J. Zhang, and Y. Ji, "Efficient deployment of aerial relays in FSO-based backhaul networks," *J. Opt. Commun. Netw.*, vol. 15, no. 1, pp. 29–42, Jan. 2023.

[9] S. R, S. Sharma, N. Vishwakarma, and A. S. Madhukumar, "HAPS-based relaying for integrated space–air–ground networks with hybrid FSO/RF communication: A performance analysis," *IEEE Trans. Aerosp. Electron. Syst.*, vol. 57, no. 3, pp. 1581–1599, Jun. 2021.

[10] T. V. Nguyen, H. D. Le, N. T. Dang, and A. T. Pham, "On the design of rate adaptation for relay-assisted satellite hybrid FSO/RF systems," *IEEE Photon. J.*, vol. 14, no. 1, pp. 1–11, Feb. 2022.

[11] H. D. Le, T. V. Nguyen, and A. T. Pham, "Aerial IRS-aided vertical backhaul FSO networks over Fisher–Snedecor F turbulence channels," in *Proc. IEEE 9th Int. Conf. Commun. Electron. (ICCE)*, Jul. 2022, pp. 133–138.

[12] T. V. Nguyen, H. D. Le, and A. T. Pham, "On the design of RIS–UAV relay-assisted hybrid FSO/RF satellite–aerial–ground integrated network," *IEEE Trans. Aerosp. Electron. Syst.*, vol. 59, no. 2, pp. 757–771, Apr. 2023.

[13] M. Choi, S. Song, D.-E. Ko, and J.-M. Chung, "Trajectory optimization for FSO based U-IoT backhaul networks," *IEEE Trans. Netw. Sci. Eng.*, vol. 10, no. 4, pp. 2030–2044, Jul. 2023.

[14] H. D. Nguyen, H. D. Let, C. T. Nguyen, and A. T. Pham, "Throughput and delay performance of cooperative HARQ in satellite-HAP-vehicle FSO systems," in *Proc. IEEE 94th Veh. Technol. Conf. (VTC-Fall)*, Sep. 2021, pp. 1–6.

[15] H. D. Le, H. D. Nguyen, C. T. Nguyen, and A. T. Pham, "FSO-based space-air-ground integrated vehicular networks: Cooperative HARQ with rate adaptation," *IEEE Trans. Aerosp. Electron. Syst.*, vol. 59, no. 4, pp. 4076–4091, Aug. 2023.

[16] H.-H. Lu, C.-Y. Li, W.-S. Tsai, P.-S. Chang, Y.-T. Chen, C.-X. Liu, T. Ko, and Y.-Y. Lin, "Simultaneous transmission of 5G MMW and sub-THz signals through a Fiber-FSO-5G NR converged system," *J. Lightw. Technol.*, vol. 40, no. 8, pp. 2348–2356, Apr. 2022.

[17] G. Park, V. Mai, H. Lee, S. Lee, and H. Kim, "Free-space optical communication technologies for next-generation cellular wireless communications," *IEEE Commun. Mag.*, to be published.

[18] H.-J. Song and N. Lee, "Terahertz communications: Challenges in the next decade," *IEEE Trans. THz Sci. Technol.*, vol. 12, no. 2, pp. 105–117, Mar. 2022.

[19] H.-B. Jeon, S.-M. Kim, H.-J. Moon, D.-H. Kwon, J.-W. Lee, J.-M. Chung, S.-K. Han, C.-B. Chae, and M.-S. Alouini, "Free-space optical communications for 6G wireless networks: Challenges, opportunities, and prototype validation," *IEEE Commun. Mag.*, vol. 61, no. 4, pp. 116–121, Apr. 2023.

[20] H. Kaushal and G. Kaddoum, "Optical communication in space: Challenges and mitigation techniques," *IEEE Commun. Surveys Tuts.*, vol. 19, no. 1, pp. 57–96, 1st Quart., 2017.

[21] H. D. Le and A. T. Pham, "Link-layer retransmission-based error-control protocols in FSO communications: A survey," *IEEE Commun. Surveys Tuts.*, vol. 24, no. 3, pp. 1602–1633, 3rd Quart., 2022.

[22] M. Alzenad, M. Z. Shakir, H. Yanikomeroglu, and M.-S. Alouini, "FSO-based vertical backhaul/fronthaul framework for 5G+ wireless networks," *IEEE Commun. Mag.*, vol. 56, no. 1, pp. 218–224, Jan. 2018.

[23] H. D. Le, V. V. Mai, C. T. Nguyen, and A. T. Pham, "Design and analysis of sliding window ARQ protocols with rate adaptation for burst transmission over FSO turbulence channels," *J. Opt. Commun. Netw.*, vol. 11, no. 5, pp. 151–163, May 2019.

[24] Y. Shoji, M. J. Fice, Y. Takayama, and A. J. Seeds, "A pilot-carrier coherent LEO-to-ground downlink system using an optical injection phase lock loop (OIPLL) technique," *J. Lightw. Technol.*, vol. 30, no. 16, pp. 2696–2706, Aug. 2012.

[25] M. A. Fernandes, P. A. Loureiro, G. M. Fernandes, P. P. Monteiro, and F. P. Guiomar, "Digitally mitigating Doppler shift in high-capacity coherent FSO LEO-to-Earth links," *J. Lightw. Technol.*, vol. 41, no. 12, pp. 3993–4001, Jun. 2023.

[26] H. D. Le, T. V. Nguyen, and A. T. Pham, "Cloud attenuation statistical model for satellite-based FSO communications," *IEEE Antennas Wireless Propag. Lett.*, vol. 20, no. 5, pp. 643–647, May 2021.

[27] K. P. Peppas, G. C. Alexandropoulos, E. D. Xenos, and A. Maras, "The Fischer–Snedecor $\mathcal{F}$-distribution model for turbulence-induced fading in free-space optical systems," *J. Lightw. Technol.*, vol. 38, no. 6, pp. 1286–1295, Mar. 2020.

[28] L. Han, X. Liu, Y. Wang, and B. Li, "Joint impact of channel estimation errors and pointing errors on FSO communication systems over $\mathcal{F}$ turbulence channel," *J. Lightw. Technol.*, vol. 40, no. 14, pp. 4555–4561, Jul. 2022.

[29] L. C. Andrews and R. L. Phillips, *Laser Beam Propagation through Random Media*, 2nd ed. Bellingham, WA, USA: SPIE Press, 2005.

[30] O. S. Badarneh, R. Derbas, F. S. Almehmadi, F. El Bouanani, and S. Muhaidat, "Performance analysis of FSO communications over F turbulence channels with pointing errors," *IEEE Commun. Lett.*, vol. 25, no. 3, pp. 926–930, Mar. 2021.

[31] X. Gao, L. Wang, X. Yu, X. Su, Y. Ding, C. Lu, H. Peng, and X. Wang, "Conditional probability based multi-objective cooperative task assignment for heterogeneous UAVs," *Eng. Appl. Artif. Intell.*, vol. 123, Aug. 2023, Art. no. 106404.

[32] X. Wang, B. Li, X. Su, H. Peng, L. Wang, C. Lu, and C. Wang, "Autonomous dispatch trajectory planning on flight deck: A search-resampling-optimization framework," *Eng. Appl. Artif. Intell.*, vol. 119, Mar. 2023, Art. no. 105792.

[33] X. Wang, Z. Deng, H. Peng, L. Wang, Y. Wang, L. Tao, C. Lu, and Z. Peng, "Autonomous docking trajectory optimization for unmanned surface vehicle: A hierarchical method," *Ocean Eng.*, vol. 279, Jul. 2023, Art. no. 114156.

KHANH D. DANG (Student Member, IEEE) is currently pursuing the B.E. degree in electronics and telecommunications with the Hanoi University of Science and Technology (HUST), Vietnam. He is actively involved in research as a member of the Communications Theory and Applications Research Group (CTARG), School of Electrical and Electronic Engineering, HUST. His research interests include optical wireless communications and cooperative HARQ for FSO-based vertical networks supporting multiple users.

HOANG D. LE (Member, IEEE) received the B.E. degree in electronics and communications from the Hanoi University of Science and Technology (HUST), Vietnam, in 2016, and the M.E. and Ph.D. degrees in computer science and engineering from The University of Aizu (UoA), Japan, in 2018 and 2021, respectively. He was a Postdoctoral Researcher with the Computer Communications Laboratory, UoA, from 2021 to 2023, where he is currently an Associate Professor with the School of Computer Science and Engineering. His current research interests include cross-layer design for optical wireless networks, hybrid FSO/RF for satellite/UAV communications, quantum cryptography, and machine learning. He is a member of ACM. He was a recipient of a number of honors/awards, including the 2018 KICS/IEEE ICTC Best Paper Award, the 2019 IEEE VTS Tokyo Chapter Young Researcher Encouragement Award, the 2019 IEEE ComSoc Sendai Chapter Student Excellent Research Award, and the 2022 IEEE ICCE Best Paper Award. He is the Young Researcher to participate in the Ninth Heidelberg Laureate Forum 2022.

CHUYEN T. NGUYEN received the B.E. degree in electronics and telecommunications from the Hanoi University of Science and Technology (HUST), Vietnam, in 2006, the M.S. degree in communications engineering from National Tsing-Hua University, Taiwan, in 2008, and the Ph.D. degree in informatics from Kyoto University, Japan, in 2013. From September to November 2014, he was a Visiting Researcher with The University of Aizu, Japan. He is currently an Associate Professor with the School of Electrical and Electronic Engineering, HUST. His current research interests include communications theory and applications with particular emphasis on protocol design for the Industrial Internet of Things applications and wireless/optical networks. He received the Fellow Award from the Hitachi Global Foundation, in August 2016, the First Best Paper Award from 2019 IEEE ICT, and the Best Paper Awards from 2018 KICS/IEEE ICTC and 2019 IEEE ICC.

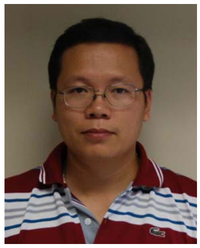

ANH T. PHAM (Senior Member, IEEE) received the B.E. and M.E. degrees in electronics engineering from the Hanoi University of Technology, Hanoi, Vietnam, in 1997 and 2000, respectively, and the Ph.D. degree in information and mathematical sciences from Saitama University, Saitama, Japan, in 2005. From 1998 to 2002, he was with NTT Corporation, Vietnam. Since 2005, he has been a Faculty Member with The University of Aizu, Aizuwakamatsu, Japan, where he is currently a Professor and the Head of the Computer Communications Laboratory, Division of Computer Engineering. He has authored or coauthored more than 200 peer-reviewed articles in his research field, which include the broad areas of communication theory and networking with a particular emphasis on modeling, design, and the performance evaluation of wired/wireless communication systems, and networks. He is also a member of IEICE and Optica.